Towards Full Resolution of Spray Breakup in Flash Atomization Conditions Using DNS

D. D. Loureiro, J. Reutzsch, A. Kronenburg, B. Weigand, and K. Vogiatzaki

Abstract Ignition of rocket thrusters in orbit requires injection of cryogenic propellants into the combustion chamber. The chamber's initial very low pressure leads to flash boiling that will then determine the dynamics of the spray breakup, the mixing of fuel and oxidizer, the reliability of the ignition and the subsequent combustion process. As details of the spray breakup process of cryogenic liquids under flash boiling conditions are not yet well understood, we use direct numerical simulations (DNS) to simulate the growth, coalescence and bursting of vapour bubbles in the superheated liquid that leads to the primary breakup of the liquid oxygen jet. Considering the main breakup patterns and droplet formation mechanisms for a range of conditions, we evaluate the effectiveness of the volume of fluid (VOF) method together with the continuum surface stress (CSS) model to capture the breakup of thin lamellae formed at high Weber numbers between the merging bubbles. A grid refinement study indicates convergence of the mass averaged droplet sizes towards an a priori estimated droplet diameter. The order of magnitude of this diameter can be estimated based on thermodynamic conditions.

D. D. Loureiro (✉) · A. Kronenburg
Institute for Combustion Technology, University Stuttgart, Stuttgart, Germany
e-mail: daniel.dias-loureiro@itv.uni-stuttgart.de

A. Kronenburg
e-mail: kronenburg@itv.uni-stuttgart.de

J. Reutzsch · B. Weigand
Institute of Aerospace Thermodynamics, University Stuttgart, Stuttgart, Germany
e-mail: jonathan.reutzsch@itlr.uni-stuttgart.de

B. Weigand
e-mail: bernhard.weigand@itlr.uni-stuttgart.de

K. Vogiatzaki
Advanced Engineering Centre, University of Brighton, Brighton, UK
e-mail: k.vogiatzaki@brighton.ac.uk

1 Introduction

Flash boiling is an important spray disintegration and mixing process in upper stage
rocket engines and orbital maneuvering systems where liquid propellants are injected
into the reaction chamber that is initially at very low pressure. Due to the low pressure
microscopic vapour bubbles spontaneously nucleate within the continuous liquid
phase and grow while the liquid continues to evaporate. The dynamics of this process
will then determine the spray breakup and the mixing of fuel and oxidizer—the latter
being important for ignition and the subsequent combustion process. Sher et al.
[20] and Prosperetti [14] provide a quite comprehensive overview of the underlying
physics and the dynamics of bubble growth under superheated conditions.

The key characteristics of a jet injected into a combustion chamber are spreading
angle, jet penetration and the resulting droplet size distribution after breakup. At
the institute of rocket propulsion at the German Aerospace Center (DLR) Lampold-
shausen high-speed shadowgraphy measurements are performed to correlate spread-
ing angle and penetration of cryogenic nitrogen and oxygen jets with the injection
conditions such as the level of superheat and the mass flow rate. Additional Phase
Doppler Anneometry (PDA) shall be used to measure droplet size and velocity distri-
butions. The temperatures for the cryogenic liquids can range from 80K to 120K and
initial chamber pressures are as low as 40 mbar. Experimental conditions thus favour
all breakup regimes from aerodynamic breakup to a fully flashing spray [7]. The lat-
ter conditions are used as a reference in this work where we focus on the microscopic
processes leading to the primary breakup of a fully-flashing liquid oxygen jet.

Methods that resolve the entire flashing chamber are usually based on Reynolds
averages or filtered values for the solution of the flow and mixing fields. These
methods focus on the macroscopic characteristics of the jet, they are, however, not
able to fully resolve the small scales of the breakup process and require closure models
for the unresolved scales. Studies using Eulerian-Lagrangian methods (cf. [4, 18])
rely on empirical models for the initial droplet size distribution and various additional
assumptions on droplet shapes and relative velocities. One fluid approaches [9, 11]
do not resolve individual bubbles and rely on mass-transfer models (such as the
homogeneous relaxation model) which require calibration. As calibration data is
scarce and most relaxation models are calibrated by using data from water flows in a
channel independent of the material system they are applied to, it seems necessary to
provide detailed (microscopic) information about size distribution of the generated
droplets, their surface area and relative velocities for cryogenic flashing sprays. Some
of these data shall now be obtained from direct numerical simulation (DNS) under
the relevant conditions. The DNS are performed on a small domain, representative
of the conditions that would be found near the exit of the injector nozzle. With
fully resolved bubbles and the introduction of phase change at the interface, we
simulate the growth, deformation and coalescence of multiple bubbles, leading to
the formation of ligaments and liquid films that breakup and burst into small droplets
that constitute the spray.

In this work, we focus on the dynamics of the breakup of thin sheets or lamellae that form in between the bubbles while they grow and interact. The bursting of lamellae will then introduce the smallest droplets present after breakup (some being physical, some being artificial and related to the mesh size), and a resolution criterion for DNS is now sought such that the artificial droplets related to the mesh size are insignificant in terms of mass and area compared to the real droplet size distribution.

2 Numerical Method

We use the in-house code Free-Surface 3D—FS3D [5] for the DNS of the atomization process. The code uses a finite volume method to discretize the incompressible Navier-Stokes equations, while capturing a fully resolved liquid-vapour interface with phase change and surface tension using the Volume of Fluid (VOF) method with PLIC reconstruction. The incompressible treatment seems justified as the low temperatures and the near vacuum pressure typical for the flashing of cryogenic liquids ensures sub-critical conditions. Here, the gas and liquid phases have a well defined interface for each individual bubble, the interface velocities are relatively low and these conditions are well suited for DNS using FS3D.

The Navier-Stokes equations are solved in a one-field formulation for a continuous velocity, $\mathbf{u}$, and pressure field, p, yielding

$$\frac{\partial}{\partial t} (\rho \mathbf{u}) + \nabla \cdot [\rho \mathbf{uu}] = \nabla \cdot \mu \left[\nabla \mathbf{u} + \nabla (\mathbf{u})^T \right] - \nabla p + \mathbf{f}_\sigma, \tag{1}$$

where $\mathbf{uu}$ is a dyadic product. Buoyancy forces have been neglected, and $\mathbf{f}_\sigma$ denotes the effects of surface tension. The latter is non-zero only in the vicinity of the interface and modeled by the continuum surface stress (CSS) model [10]. In the VOF method an additional variable is transported representing the volume fraction of liquid in the cell, f, with $f = 1$ in the liquid phase, $f = 0$ in the gas phase and $0 < f < 1$ in cells containing the interface. Volume-averaged properties are then defined as $\rho = \rho_\ell f + \rho_v (1 - f)$ for the density and $\mu = \mu_\ell f + \mu_v (1 - f)$ for viscosity, where the subscripts ℓ and v denote the liquid and vapour phases. Constant temperature and incompressibility are assumed within each phase thus ρ_ℓ and ρ_v are constants, as well as μ_ℓ and μ_v. The f transport equation can be written as [17]

$$\frac{\partial f}{\partial t} + \nabla \cdot (f \mathbf{u}_\Gamma) = \frac{\dot{m}'''}{\rho_\ell}, \tag{2}$$

where $\mathbf{u}_\Gamma$ is the interface velocity and $\dot{m}'''$ is the liquid evaporation rate at the interface. The latter can be defined as $\dot{m}''' = a_\Gamma \dot{m}''$, using the evaporation mass flux, $\dot{m}''$, and the interface density, a_Γ, which represents the interface area per unit of volume. A PLIC (piecewise linear interface calculation) scheme [15] is used to determine the interface plane for each finite volume cell, and the exact position of the interface within the

cell is determined by matching the volume bound by the plane with the volume fraction f. The PLIC reconstruction coupled with the CSS model for surface tension is a flexible approach that requires only moderate resolution when modeling bubble coalescence, liquid breakup and droplet collisions. However, during bubble merging thin lamellae will form, and unphysical dynamics of the interactions between the two interfaces of a thin lamella may be predicted if the lamella thickness is smaller than 4 computational cells [12]. This corresponds to the width of the stencil around the interface used to calculate $\mathbf{f}_\sigma$ and is responsible for some of the mesh dependent effects analysed in this work. The pressure field, p, is obtained implicitly by solving the pressure Poisson equation

$$\nabla \cdot \left[\frac{1}{\rho} \nabla p \right] = \frac{\nabla \cdot \mathbf{u}}{\Delta t}, \tag{3}$$

using an efficient multi-grid method [16]. Continuity is implied in the velocity divergence term, with $\nabla \cdot \mathbf{u} = 0$ except in interface cells (with $0 < f < 1$). There, $\nabla \cdot \mathbf{u}$ is determined to account for phase change with large density ratio as a function of the evaporation rate, $\dot{m}'''$, using the method detailed in [17] which ensures mass conservation in spite of a volume averaged density, ρ, being used. This naturally introduces the jump condition in the momentum conservation equation through the pressure field, p.

While DNS resolves all hydrodynamically important scales, it cannot capture the molecular processes at the interface that determine the evaporation rate. Phase change continues to require modeling. Here, we model the unknown $\dot{m}''$ according to the growth rate of a spherical bubble,

$$\dot{m}'' = \rho_v \dot{R}, \tag{4}$$

where $\dot{R}$ acts as an imposed interface velocity and is obtained from a numerical solution as presented by Lee and Merte [11]. They coupled the Rayleigh-Plesset equation with heat transfer at the bubble interface. This solution can provide evaporation and growth rates during all stages of the bubble growth while analytical solutions [19] that were favoured in the past, cover the heat diffusion driven stage only [2]. It should be noted that for the conditions analysed in this work the interface velocities are in the order of 10 m/s which ensures a low Mach number in the gas. However, due to the effect of varying vapour pressure in the early stages of bubble growth, the vapour density can vary substantially which is not captured with the current numerical approach. However, both $\dot{R}$ and ρ_v are calibrated to the bubble size at which the bubble merging occurs, as detailed in Sect. 3, which accounts the for the influence of interface cooling and vapour compressibility effects in the bubble growth up to that point. This provides an adequate approximation for the volume of vapour being generated at the interface, while the dynamics of the subsequent bubble breakup are captured by DNS with the assumption of constant fluid properties.

3 Computational Setup

As detailed in [13], the simulation domain represents a small volume of continuous liquid near the exit of the injector nozzle when flash boiling starts. For the current setup, no assumptions are necessary regarding bubble distribution or the type of interface instability leading to breakup. Nonetheless, regular arrays of equally spaced bubbles are used here for simplicity of setup, for repeatability of results and for a reduction in system parameters that allow for a better systematic comparison of different setup conditions (for a general impression compare e.g. Fig. 2 top left).

The initial relative velocity between bubbles and liquid is zero emulating a fluid element moving with bulk velocity. The liquid is free to expand through the use of continuity boundary conditions (outflow) and large buffer zones are used to prevent the interaction of the liquid-vapour interface with the boundaries. Finally, symmetry conditions are used to reduce the computational cost. The reference liquid temperature and ambient pressure conditions for the DNS, T_∞ and p_∞, correspond to values given in the experiments at DLR. The initial spacing between the bubbles is assumed to be uniform and should be related to the nucleation rate J and the mass flow rate. Since here a mass flow rate is not defined, such dependence is avoided and the bubble spacing is treated as a free geometric parameter and can represent different nucleation rates triggered by different levels of disturbances in the flow. As such, we define the parameter R_f as the final bubble radius at which the bubbles are expected to touch and start merging. Considering p_∞ and T_∞, we use the critical radius as a reference value and normalize R_f, $R_f^* = R_f/R_{\mathrm{crit}}$. The normalized quantity represents a growth factor since nucleation with R_{crit} given by $R_{\mathrm{crit}} = 2\sigma/(p_{\mathrm{sat}}(T_\infty) - p_\infty)$. Here, σ denotes the surface tension at T_∞. With the parameters p_∞ and T_∞, we use the Lee and Merte solution [11] for single bubble growth to determine the growth rate, $\dot{R}$, vapour density ρ_v, surface tension, σ, and vapour viscosity, μ_v, as functions of R_f^*. The density and viscosity of the liquid, ρ_ℓ and μ_ℓ, are functions of p_∞ and T_∞ and obtained from the equation of state library CoolProp [3].

3.1 Characterization of the Flow

Droplet dynamics are usually characterized by the Weber (We) and Ohnesorge (Oh) numbers. For a corresponding definition applicable to bubble dynamics we use the interface velocity, $\dot{R}$, and the final bubble diameter, $2R_f$, as characteristics scales and define

$$\mathrm{We}_b = \frac{\rho_\ell \dot{R}^2 2R_f}{\sigma},\tag{5}$$

and

$$\mathrm{Oh}_b = \frac{\mu_\ell}{\sqrt{\rho_\ell \sigma 2R_f}},\tag{6}$$
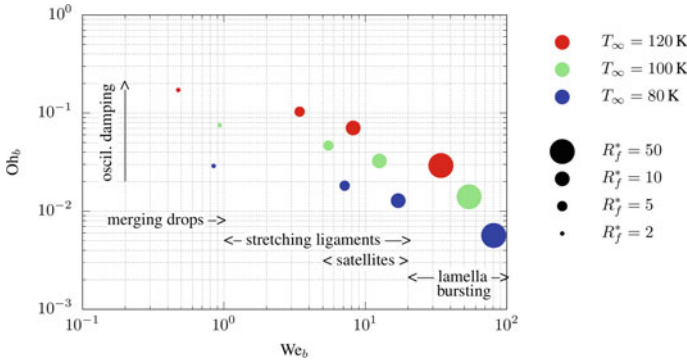
Fig. 1 Weber-Ohnesorge diagram to characterize the type of breakup

with subscript b indicating the characteristic numbers for bubbles. The Weber-Ohnesorge diagram (Fig. 1) shows the characteristic quantities for all DNS simulations that were part of the study.

Loureiro et al. [13] identified very distinct types of breakup that are also indicated in the diagram. These types are primarily determined by the We_b number while Ohnesorge number is typically below 1, but the larger Oh_b the stronger the damping of droplet oscillations due to larger viscous effects.

For cases located in the small Weber number regime ($We_b < 5$), surface tension forces dominate the bubble dynamics during merging and the interstitial liquid between the bubbles does not break into smaller droplets but coalesces generating relatively large droplets relative to the bubble size (cf. Fig. 2a). Cases with $We_b \sim \mathcal{O}(10)$ result in a binary droplet distribution of main droplets and satellites, where the size of the main droplets matches the interstitial volume $D \approx 1.94R_f$ (Fig. 2b and c). In this regime the larger Oh_b (Fig. 2b) leads to more stable main droplets and smaller or no satellites. Finally, as depicted in Fig. 2d and e, cases with $We_b > 20$ show large deformation of the bubbles prior to merging, forming thin and flat liquid lamella between them. As the bubble continues to grow, the lamellae stretc.h and thin until they can no longer be properly resolved by the computational mesh, potentially generating a large number of artificial droplets.

3.2 Test Cases

For the mesh sensitivity studies we focus on two cases with $T_\infty = 120K$ (case A) and $T_\infty = 80K$ (case B) and $p_\infty = 1000Pa$. The two cases represent the two extrema of injection temperatures at the minimum vacuum pressure as realised in the experiments at DLR. The Weber numbers are between 30 and 100 and the test cases are therefore located in the "lamella bursting" regime indicated in Fig. 1. Each setup simulates the dynamics of 3^3 bubbles with details of the computational parameters
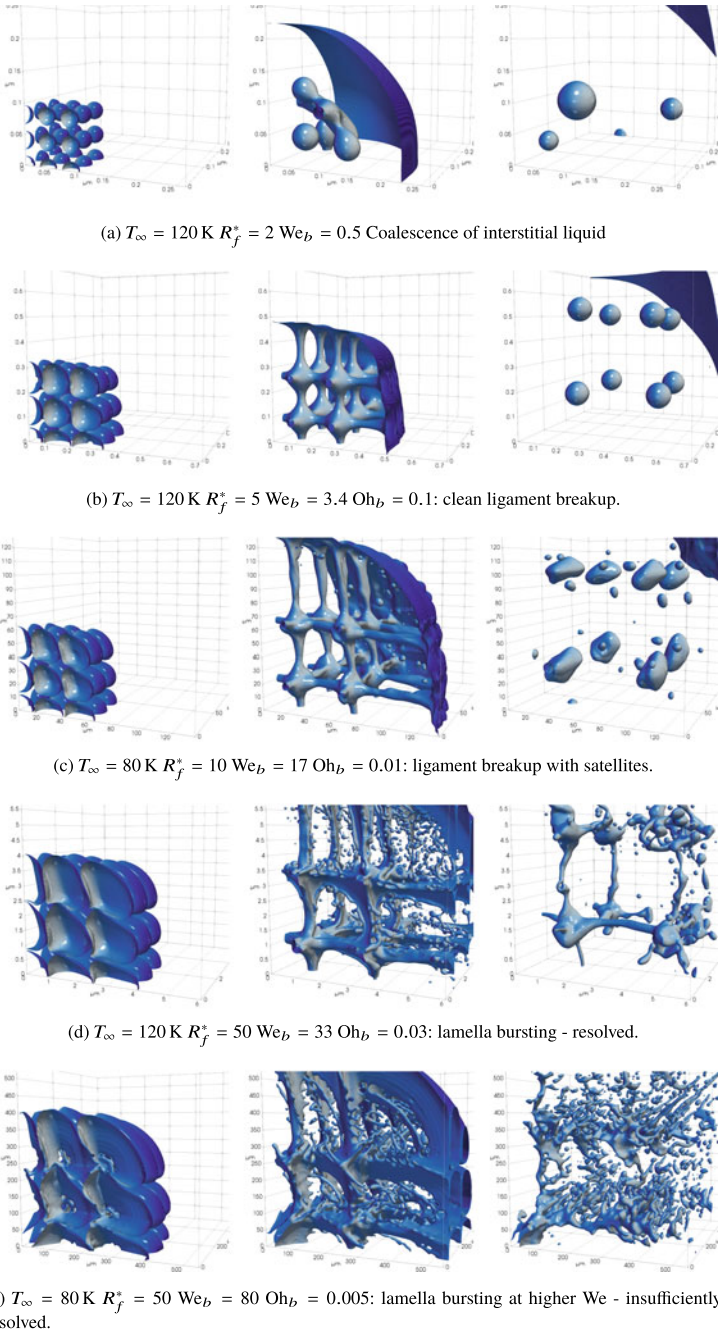
(a) $T_\infty = 120\,\text{K}$ $R_f^* = 2$ $We_b = 0.5$ Coalescence of interstitial liquid

(b) $T_\infty = 120\,\text{K}$ $R_f^* = 5$ $We_b = 3.4$ $Oh_b = 0.1$: clean ligament breakup.

(c) $T_\infty = 80\,\text{K}$ $R_f^* = 10$ $We_b = 17$ $Oh_b = 0.01$: ligament breakup with satellites.

(d) $T_\infty = 120\,\text{K}$ $R_f^* = 50$ $We_b = 33$ $Oh_b = 0.03$: lamella bursting - resolved.

(e) $T_\infty = 80\,\text{K}$ $R_f^* = 50$ $We_b = 80$ $Oh_b = 0.005$: lamella bursting at higher We - insufficiently resolved.

Fig. 2 Time series for different breakup patterns under flashing conditions

Table 1 Simulation parameters and grid refinement levels

Case	A	B	C (Control)
T_∞	120K	80K	120K
p_∞	1000Pa	1000Pa	1000Pa
ΔT	58.71K	18.71K	58.71K
R_p	1022	30.12	1022
R_f^*	50	50	175
R_{crit}	0.012μm	1.01μm	0.012μm
We_b	33	80	80
Oh_b	2.9×10^{-2}	5.66×10^{-3}	1.5×10^{-2}
D_{ref}	0.285μm	10.77μm	0.418μm
128^3 grid			
$\Delta x = R_f/14$	4.2×10^{-8}m	3.8×10^{-6}m	1.5×10^{-7}m
256^3 grid:			
$\Delta x = R_f/28$	2.1×10^{-8}m	1.9×10^{-6}m	7.4×10^{-1}m
512^3 grid:			
$\Delta x = R_f/57$	1.1×10^{-8}m	9.5×10^{-7}m	3.7×10^{-8}m
1024^3 grid:			
$\Delta x = R_f/114$	5.3×10^{-9}m	–	–

given in Table 1. The physical conditions for flash atomization are typically charac-
terized by p_∞, T_∞, the superheat and the pressure ratio. The level of superheat is
defined by $\Delta T = T_\infty - T_{\text{sat}}(p_\infty)$, or in terms of pressure as $R_p = p_{\text{sat}}(T_\infty)/p_\infty$.

As the Weber numbers of cases A and B are similar, we can expect the same type
of breakup pattern, but length scales are vastly different as a result of the difference
in T_∞. The table includes a third case, labeled case C, that matches We_b of case B but
uses a higher injection temperature, $T_\infty = 120$K. The case corroborates the results'
independence of Oh_b, the thermodynamic conditions and length scales and results
are not shown here for brevity of presentation.

One key issue for spray breakup is the resolution requirement, i.e. the expected
minimum droplet that needs to be resolved after spray breakup. The literature on
DNS of droplet break up has shown that as the Weber number is increased more
"smaller" droplets are expected and thus a higher resolution is required. However,
if DNS is expected to act in a predictive manner, an a priori criterion needs to be
established in order to define the necessary resolution. Such a criterion is currently
missing from existing literature. Here, we equate the droplet's volumetric surface
energy, $4\sigma/D_{\text{ref}}$, with the available kinetic energy in the liquid, $\rho_\ell \dot{R}^2/2$, yielding

$$D_{\text{ref}} \approx \mathcal{O}\left(\frac{8\sigma}{\rho_\ell \dot{R}^2}\right). \tag{7}$$

This value shall be understood as an order of magnitude estimate for the prediction of mesh resolution requirements and not as an exact formula for the smallest droplet size. The real minimum droplet diameter may deviate since $\dot{R}$ considers a local interface velocity of a single bubble only and bubble interactions and convective effects may alter the local (relevant) kinetic energy that leads to breakup.

4 Results

The spray breakup includes bubble growth, merging of the bubbles, formation of thin lamellae and shedding of droplets from the thin lamellae. The later stages of the lamellae formation and droplet shedding are shown in Figs. 3 and 4 for cases A and B, respectively. The "open" area between the liquid is where the bubbles have already merged and the liquid between the bubbles is now being pushed back and retracting due to continuous growth of the bubbles and movement of the outer surface. Due to the inertia of the liquid between the bubbles, the fluid does not fully retract immediately, but relatively flat thin liquid layers, the lamellae, persist. The retracting velocity of the lamellae is relatively fast and instability at the rim of the lamella leads to the shedding of droplets.

The subfigures in Figs. 3 and 4 show the effect of grid refinement. For all simulations, the estimated minimum droplet size D_{ref} is resolved by a minimum of 6 (case A) and 3 (case B) CFD cells. Some effects of grid resolution on breakup dynamics and droplet size can be observed. For case A (Fig. 3) the lamella seems to be more stable with increasing resolution, leading to a delay in the droplet formation. Most notably, the lower resolutions promote the ideas of breakup of a liquid rim due to longitudinal instability [1]. "Liquid finger" formation with subsequent droplet breakup seems to be the dominant breakup mechanism. However, finer resolutions seem to dampen the finger formation and the rim itself detaches from the lamella. For case B (Fig. 4) the droplets generated by lamella breakup seem to be well resolved and stable with increasing resolution. However, their number and size still changes between the 256^3 grid and 512^3 grid and further computations with 1024^3 grid nodes may be needed for a last conclusive assessment.

4.1 Statistical Analysis

It has been questioned in the past whether mesh independence can ever be achieved by simple mesh refinement [12] for droplet collision problems. It may be more important to achieve convergence of the mass weighted droplet size distribution, i.e. a decrease of the minimum droplet size with increased mesh resolution is accepted but these smallest droplets shall not significantly affect the mass balance and can thus be ignored.
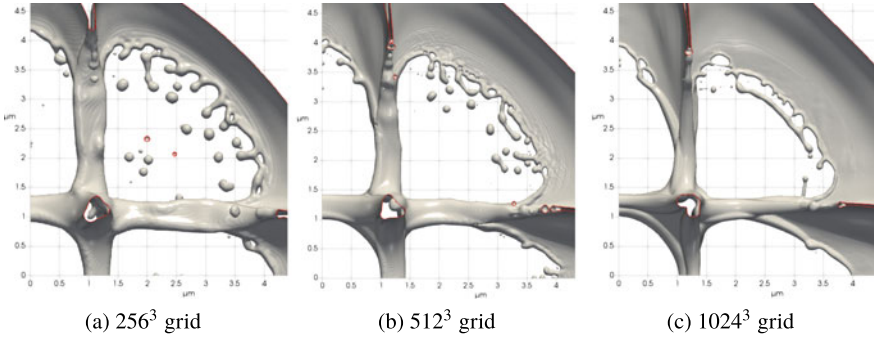
(a) 256^3 grid (b) 512^3 grid (c) 1024^3 grid

Fig. 3 Case A breakup patterns for different grid refinements at simulation time $t = 0.1\mu$s. The lamellae are represented by the iso-surface $f = 0.1$
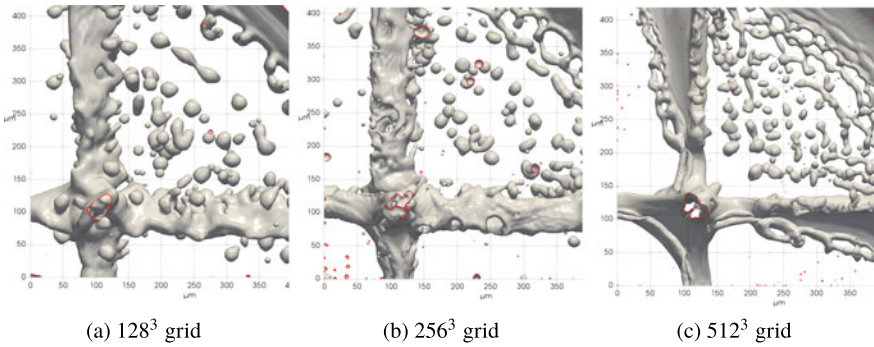

(a) 128^3 grid (b) 256^3 grid (c) 512^3 grid

Fig. 4 Case B breakup patterns for different grid refinements at simulation time $t = 0.58\mu$s. The lamellae are represented by the iso-surface $f = 0.1$

To sample the statistics a filter is applied such that only fully atomized (stable) droplets are counted and large ligaments or any residual droplets that fall below the resolution criterion and are not fully resolved are excluded. Representative diameters such as the arithmetic mean D_{10}, the Sauter mean D_{32} or the De Brouckere mean diameter $D_{43} = \sum_{i \in j}^{N_j} D_i^4 / \sum_{i \in j}^{N_j} D_i^3$, the latter corresponds to the mass-weighted mean of the spray, are then computed from these droplets. The dependence of these representative diameters on the mesh refinement is shown in Fig. 5. Both cases indicate convergence of the Sauter and De Brouckere means, and a resolution with 512^3 nodes seems sufficient to capture the droplet size of the droplets holding most of the liquid mass after breakup. The percentages indicate the deviation of D_{43} from the corresponding value at the finest mesh and should be understood as order of magnitude analysis as data are extracted from one instant in time and the exact values are likely to change somewhat during the course of the breakup. The larger sensitivity of D_{10} is due to the generation of a large number of artificial, small droplets. This is expected and has been documented in the archival literature. The figure also indicates the estimate for the minimum droplet size, D_{ref} (Eq. 7) . For case B the size of the
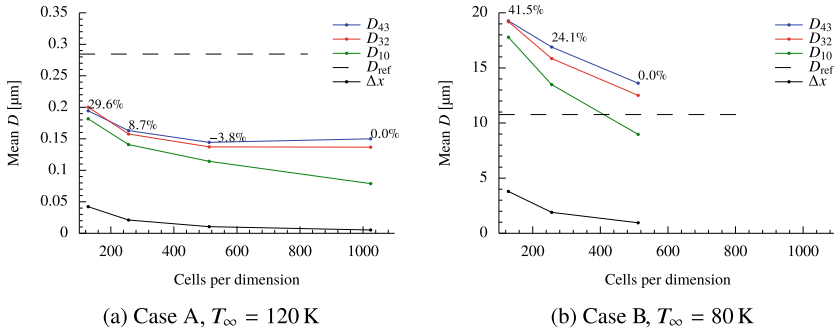
Fig. 5 Dependency of the D_{10} (arithmetic), D_{32} (Sauter) and D_{43} (De Brouckere) mean diameters with the mesh refinement for both cases studied and comparison with the cell size Δx and estimated droplet size D_{ref} (Eq. 7). For the D_{43} the percentage of the variation relative to the most refined case is shown

main droplet group seems to converge towards this value and for case A, the resulting droplets are—on average—half the size of D_{ref}. The good agreement for case B may be somewhat fortuitous, but both cases indicate that D_{ref} may provide a suitable first estimate for the mesh size needed for adequate resolution.

The normalized droplet size distributions shown in Fig. 6 provide a more quantitative measure and demonstrate more clearly the dependence of the droplet sizes on grid resolution with the presence of smaller droplets for the cases with higher resolution. Also, a bimodal droplet distribution is observed, with a clear segregation between one group of larger droplets that represents "physical" droplets after breakup and the much smaller, artificial satellite droplets. However, Fig. 6 should be seen in conjunction with Fig. 7 that shows the distribution of mass-weighted droplet diameters. It is apparent that the distribution of volume fraction (here equivalent to the mass weighted average) does not change much with resolution for case A (256^3 grid nodes gives a similar picture and only a coarser mesh with 128^3 grid nodes provide notably larger droplets) while case B seems to converge to the estimated D_{ref} for 512^3 grid nodes and a resolution requirement of $\Delta x \approx D_{ref}/10$ may be a reasonable criterion for the prediction of the smallest (but relevant) droplet sizes being generated during a flash boiling process.

It should be noted that the convergence of the macroscopic averaged quantities has been shown e.g. for splashing by Gomaa et al. [8] in 2008. So the here obtained results are perfectly in line with this investigation.

4.2 Computational Performance

The general performance of FS3D on the Cray XC40 Hazel-Hen super computer located at the High Performance Computing Center Stuttgart (HLRS) has previously
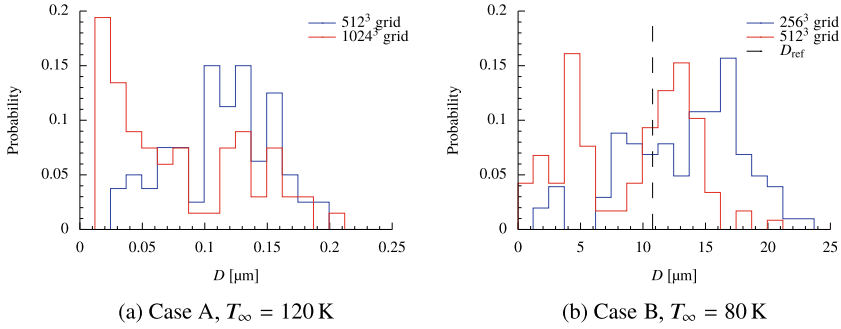
Fig. 6 Discrete probability density functions (PDF) of the equivalent droplet diameter D_i for cases A and B at the two highest levels of mesh refinement for each case
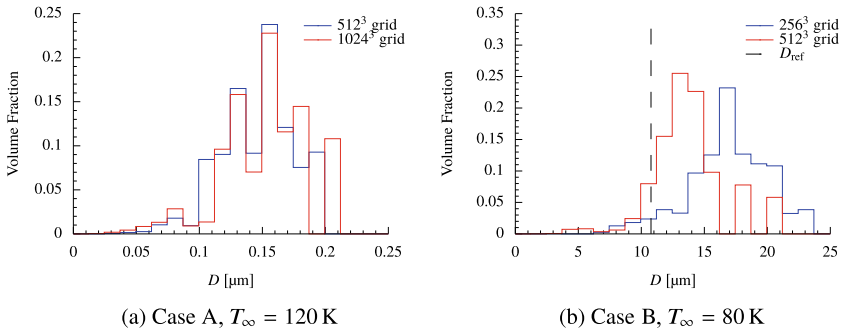

Fig. 7 Discrete volume fraction distribution function of the equivalent droplet diameter D_i for cases A and B at the two highest levels of mesh refinement for each case

been analysed in various works such as such as [6]. However, specific case configurations can affect the parallelization efficiency and the issue of efficient implementation needs to be revisited. Also note that the code allows for hybrid parallelization using MPI and OpenMP, but only MPI has been used for this study.

The largest case with 1024^3 grid nodes is the maximum mesh size that should be used on Hazel-Hen according to weak-scaling limitations of FS3D reported in [6]. Therefore, only the strong scaling efficiency is tested here. The test is based on case A with 1024^3 nodes while the number of processors has been varied. The domain is initialized with an array of 5^3 bubbles that are partially overlapping. This scenario is similar to the conditions when bubbles start to coalescence. The fluid properties and the bubble size/spacing is taken from case A as given in Table 1. The resolution of the bubbles at time of merging is about 100 cells per bubble diameter.

Memory requirements and significant initialization times limit the range for the number of processors, N_{proc}, that shall be used: here N_{proc} varies from 512 to 8192 distributed on compute nodes with 24 processors each. All relevant details are given in Table 2. The computational speed (in cycles per hour) is determined by the total

Fig. 8 Results for strong-scaling on the for the 1024^3 grid: Compute speed compared to ideal linear scaling and scaling efficiency (annotations)
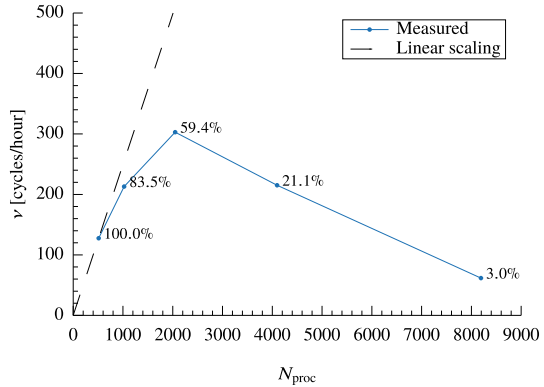
computation time (wall time) minus the initialization time divided by a fixed number of time-steps (cycles), viz.

$$\nu = \frac{t_{\text{total}} - t_{\text{init}}}{N_{\Delta t}}. \tag{8}$$

The number of time-steps, $N_{\Delta t}$, was set to 20 for all the cases and care has been taken that the number of iterations of the pressure solver for each time step are comparable. The strong-scaling efficiency is given by the ratio of the total computational cost per time step relative to the reference value using 512 processors,

$$\eta = \frac{N_{\text{proc}}/\nu}{512/\nu_{512}} \times 100\%. \tag{9}$$

Figure 8 shows the computational speed, ν, as a function of N_{proc}. The annotated percentages indicate the corresponding efficiency η for each case. The peak performance is measured for $N_{\text{proc}} = 2048$ which corresponds to a load of $64 \times 64 \times 128$ cells per processor. This only marginally differs from earlier results [6] that report peak performances for 64^3 cells/processor on a 512^3 grid, and results are consistent with a reported 20% weak-scaling efficiency at $N_{\text{proc}} = 4096$.

Computational requirements for the cases as reported in Sect. 3 can now be given: case A with 1204^3 grid nodes requires 16600 cycles for a physical simulation time of 0.14μs. With $N_{\text{proc}} = 2048$, the simulation time may be as low as 55 h with a total cost of 1.1×10^5 processor-hours. However, the number of iterations of the pressure solver can vary significantly, especially upon topological changes and the formation of complex interface structures. For case A the number of iterations varies by a mere 20% and computational costs are therefore very moderate. In contrast, the complexity of breakup is much larger for case B and the number of iterations by the pressure solver can be up to two orders of magnitude higher. This effectively halts simulations when breakup occurs and explains the omission of results of case B with 1024^3 nodes. Larger computations are to be conducted in future but may require some improvement of the iterative pressure solver for the specific time steps when bubble merging occurs.

Table 2 strong-scaling cases and results for 1024^3 grid

N_{proc}	Nodes	Cells/proc.	ν (cycles/hour)	η (efficiency)
512	22	128x128x128 = 2097152	128	100%
1024	43	64x128x128 = 1048576	213	83%
2048	86	64x 64x128 = 524288	303	59%
4096	171	64x 64x 64 = 262144	215	21%
8192	342	32x 64x 64 = 131072	62	3%

5 Conclusions

The dynamics of breakup and droplet formation under flashing conditions have been investigated. The relevant parameter range as defined in corresponding experiments carried out at the DLR institute of rocket propulsion Lampoldshausen has been covered, but the focus of this work has been on the high Weber number cases as they present the most challenging conditions on grid resolution for capturing all the dynamic processes that determine the final droplet size distribution.

The smallest scales are expected to be located between the bubbles when they merge. There, thin lamellae are formed and droplets are formed at the rim of these lamellae by either "finger"-formation and subsequent droplet pinch-off or by break-off of the entire rim. This disintegration of the lamellae is expected to yield the smallest droplets, let them be of physical or artificial (mesh resolution induced) size. A mesh refinement study corroborates existing studies inasmuch the minimum droplet size decreases with increasing resolution and seems to be mesh dependent. However, the mass weighted droplet diameter tends to converge towards a given size that can be estimated by analysis of surface and kinetic energy acting on the bubble walls. The exact average droplet diameter may deviate from this estimate by a factor of two, however, an increase in resolution also demonstrates that the overall liquid mass associated with lamellae breakup approaches single digit percentage values and the highest resolution may not be needed for adequate approximation of the entire spray breakup process.

The dynamics of the lamella puncture and retraction are exposed, as well as their dependence on the mesh resolution. This can be used as a criterion to determine the significance of different size groups of the final droplet size distributions or to define a minimum resolution requirement to capture the bursting of lamellae in the high Weber number range. The current DNS therefore demonstrates that (1) the dynamics of the breakup influence the characteristics of droplet formation and droplet sizes, and (2) the current DNS implementation can be used for simulations of much larger domains that will then capture the complete spectrum of the droplet size distributions resulting from a flashing jet.

References

1. G. Agbaglah, C. Josserand, S. Zaleski, Longitudinal instability of a liquid rim. Phys. Fluids **25**(2), 022103 (2013). https://doi.org/10.1063/1.4789971
2. R. Bardia, M.F. Trujillo, Assessing the physical validity of highly-resolved simulation benchmark tests for flows undergoing phase change. Int. J. Multiphase Flow **112** (2018). https://doi.org/10.1016/j.ijmultiphaseflow.2018.11.018
3. I.H. Bell, J. Wronski, S. Quoilin, V. Lemort, Pure and pseudo-pure fluid thermophysical property evaluation and the open-source thermophysical property library coolprop. Ind. Eng. Chem. Res. **53**, 2498–2508 (2014). https://doi.org/10.1021/ie4033999
4. R. Calay, A. Holdo, Modelling the dispersion of flashing jets using cfd. J. Hazard. Mater. **154**(1–3), 1198–1209 (2008)
5. K. Eisenschmidt, M. Ertl, H. Gomaa, C. Kieffer-Roth, C. Meister, P. Rauschenberger, M. Reitzle, K. Schlottke, B. Weigand, Direct numerical simulations for multiphase flows: an overview of the multiphase code FS3D. J. Appl. Math. Comput. **272**(2), 508–517 (2016)
6. M. Ertl, J. Reutzsch, A. Nägel, G. Wittum, B. Weigand, Towards the implementation of a new multigrid solver in the dns code fs3d for simulations of shear-thinning jet break-up at higher reynolds numbers, in *High Performance Computing in Science and Engineering ' 17* Springer International Publishing (2018), pp. 269–287
7. J.W. Gaertner, A. Rees, A. Kronenburg, J. Sender, M. Oschwald, D. Loureiro, Large eddy simulation of flashing cryogenic liquid with a compressible volume of fluid solver, in *ILASS–Europe 2019, 29th Conference on Liquid Atomization and Spray Systems* (2019)
8. H. Gomaa, B. Weigand, M. Haas, C. Munz, Direct Numerical Simulation (DNS) on the influence of grid refinement for the process of splashing, in *High Performance Computing in Science and Engineering '08 Transactions of the High Performance Computing Center, Stuttgart (HLRS)* (2008), pp. 241–255
9. I. Karathanassis, P. Koukouvinis, M. Gavaises, Comparative evaluation of phase-change mechanisms for the prediction of flashing flows. Int. J. Multiph. Flow **95**, 257–270 (2017)
10. B. Lafaurie, C. Nardone, R. Scardovelli, S. Zaleski, G. Zanetti, Modelling merging and fragmentation in multiphase flows with surfer. J. Comput. Phys. **113**(1), 134–147 (1994)
11. H.S. Lee, H. Merte, Spherical vapor bubble growth in uniformly superheated liquids. Int. J. Heat Mass Transf. **39**(12), 2427–2447 (1996)
12. M. Liu, D. Bothe: Numerical study of head-on droplet collisions at high weber numbers. J. Fluid Mech. **789**, 785–805 (2016). https://doi.org/10.1017/jfm.2015.725
13. D. Loureiro, J. Reutzsch, D. Dietzel, A. Kronenburg, B. Weigand, K. Vogiatzaki, DNS of multiple bubble growth and droplet formation in superheated liquids, in *14th International Conference on Liquid Atomization and Spray Systems* ,Chicago, IL, USA (2018)
14. A. Prosperetti, Vapor bubbles. Ann. Rev. Fluid Mech. **49** (2017)
15. W.J. Rider, D.B. Kothe, Reconstructing volume tracking. J. Comput. Phys. **141**(2), 112–152 (1998)
16. M. Rieber, Numerische modellierung der dynamik freier grenzflachen in zweiphasenstromungen. Ph.D. thesis, Universitat Stuttgart (2004)

17. J. Schlottke, B. Weigand, Direct numerical simulation of evaporating droplets. J. Comput. Phys. **227**, 5215–5237 (2008)
18. R. Schmehl, J. Steelant, Computational analysis of the oxidizer preflow in an upper-stage rocket engine. J. Propul. Power **25**(3), 771–782 (2009)
19. L. Scriven, On the dynamics of phase growth. Chem. Eng. Sci. **10**(1), 1 – 13 (1959). https://doi.org/10.1016/0009-2509(59)80019-1
20. E. Sher, T. Bar-Kohany, A. Rashkovan, Flash-boiling atomization. Prog. Energy Combust. Sci. **34**, 417–439 (2008)